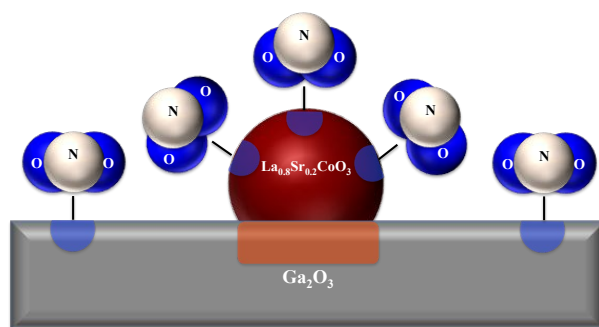Journal of
Materials Chemistry A

Perovskite-Sensitized β-Ga2O3 Nanorod Arrays for Highly Selective and Sensitive NO2 Detection at High Temperature

Journal:	*Journal of Materials Chemistry A*
Manuscript ID	TA-ART-03-2020-002691.R2
Article Type:	Paper
Date Submitted by the Author:	06-May-2020
Complete List of Authors:	Zhang, Bo; University of Connecticut Lin, Hui-Jan; Institute of Materials Science, Department of Materials Science and Engineering Gao, Haiyong; University of Connecticut, Lu, Xingxu; University of Connecticut, Department of Materials Science and Engineering Nam, Chang-Yong; Brookhaven National Laboratory, Center for Functional Nanomaterials Gao, Pu-Xian; University of Connecticut,

SCHOLARONE™
Manuscripts

The thermally-stable perovskite (La, Sr)CoO$_3$ (LSCO) nanoparticles significantly enhance the NO$_2$ gas sensitivity of wide-bandgap β-Ga$_2$O$_3$ nanorod arrays at 800 °C. The p-n junction formed in the LSCO/Ga$_2$O$_3$ interface plays an important role in improving the gas sensor performance.

ARTICLE

Perovskite-Sensitized β-Ga₂O₃ Nanorod Arrays for Highly Selective and Sensitive NO₂ Detection at High Temperature

Bo Zhang, [a, †] Hui-Jan Lin, [a, †] Haiyong Gao, [a] Xingxu Lu, [a] Chang-Yong Nam, [b] Pu-Xian Gao [*, a]

Amongst various gaseous pollutants, NO₂ is one of the major exhausts originating from fossil fuel and gas combustions in vehicle engines and power plants at high temperature. Under such scenario, *in situ* and real-time gas detection and monitoring solutions are largely limited, which hinders the energy-efficient and resource-saving operations of these advanced energy systems. In this report, a new type of perovskite-sensitized β-Ga₂O₃ nanorod-array has been successfully fabricated to detect NOₓ at high temperature selectively and sensitively. The demonstrated gas sensors are highly sensitive to NO₂ at 800 °C, with excellent reversible and reproducible response characteristics. Through the surface decoration of perovskite-type La₀.₈Sr₀.₂CoO₃ (LSCO) nanoparticles, the sensitivity of β-Ga₂O₃ nanorod array gas sensors is enhanced by nearly an order of magnitude, along with much faster response dynamics. A remarkable selectivity toward oxidative gases was also demonstrated with the robust differentiation of NO₂.

Introduction

High-temperature gas sensing has played a significant role in monitoring, control, and efficient operation of various energy production and chemical processing routes. Typical examples include, but not limited to, operations of combustion engines, boilers, gasifiers, as well as turbines, and the emission and process control during the combustion processes involving these systems and other industrial chemical processes.[1-3] Such processes usually emit the major atmospheric pollutants including CO, hydrocarbons (HCs), SOₓ, and NOₓ due to the high temperature combustions.[4] Amongst these emissions, NOₓ has been named one of the major challenges toward establishing a sustainable global environment.[5] It is noted that exhaust or feed processing temperatures can reach up to 800 °C during combustions in close proximity to the engines or combustors.[6] Current commercial sensing and monitoring approaches including calorimetry, chromatography, and spectroscopic techniques are less cost-effective and space consuming for *in-situ* and on-board measurements. In this regard, solid-state gas sensors present an alternative option for harsh environment gas detection. At present, solid state gas sensors operated at high temperature face tremendous challenges,

including thermal and long-term stability, detection limit, reproducibility, and selectivity. Specifically, the high temperature and highly corrosive environment may degrade the sensing materials and even irreversibly destroy the reproducibility. Besides, usually weak adsorption of gaseous analytes at high temperature may hinder a high sensitivity towards analytes in ppm quantities. Thus, suitable gas sensors with careful material choice and structure design are urgently demanded at high temperature for monitoring combustion processes at low cost.[7-10]

The detection and monitoring of NO and NO₂ are usually required in automotive engines combustion and industrial after-treatment systems.[11-13] The sensors in this case must be able to work at high temperatures above 500 °C considering the typical engine combustion process taking place at high temperatures. However, most reported solid-state NOₓ sensors can operate only at temperatures ranging from room temperature to 300 °C [14, 15], and up to 500 °C[12, 16, 17]. These reported sensors displayed good NO₂ response at ~ 200–400 °C, but tend to lose sensitivity and function at higher temperatures. Meanwhile, various strategies can be applied to improve the performance of sensory material, such as doping,[18, 19] surface functionalization,[20-24] and use of heterojunctions.[25-28]Among these, the surface decoration of catalytically active noble metal particles over the active sensor material has been one of the most effective techniques used widely in practice. However, the prohibitive nature of noble metals due to their scarcity as well as their limited high-temperature stability resulting from sintering effect are two ongoing hurdles for their commercial utilization at high temperature.[29] Alternatively, perovskite oxide nanoparticles are good candidates for replacing noble metals due to their low cost and ease in synthesis; recently

ᵃ· *Department of Materials Science and Engineering & Institute of Materials Science, University of Connecticut, 97 North Eagleville Road, Storrs, Connecticut 06269-3136, United States*

ᵇ· *Centre for Functional Nanomaterials, Brookhaven National Laboratory, Upton, New York 11973, United States*

† *Equal contribution authors*

* *E-mail: puxian.gao@uconn.edu*

we discovered that the surface decoration of perovskite nanoparticles could enhance the CO sensing performance of Ga_2O_3-nanorod-array-based conductometric gas sensors at 500 °C.[30] In addition, perovskite oxides have been known as an important class of functional materials exhibiting remarkable physical and chemical properties as in high temperature superconductors,[31-33] colossal magneto-resistant manganites, and high/medium-temperature solid oxide fuel cells.[34, 35]

Wide bandgap semiconductors have been widely adopted in solid state sensors and electronics. In the past few years, a ramping research interest has been paid on the ultra-wide bandgap oxide semiconductors such as gallium oxide (Ga_2O_3). This is a chemically and thermally stable metal oxide semiconductor with a wider band gap (~4.9 eV) than ones in typical metal oxides such as ZnO (~3.2 eV) and SnO_2 (3.8 eV). In comparison to other non-oxide systems (e.g., AlGaN, AlN, GaN), Ga_2O_3 possesses the largest band gap and could be grown in large volume(>1 kg) with good crystalline structure.[36] Owing to its large band gap and high visible light transparency, the Ga_2O_3 has shown a good potential as the next generation candidates as photo detectors.[37-39] Besides, wide-band gap semiconductors are efficient and can also handle a high power with superior power conversion efficiency. For example, a novel hybrid structure of graphene/Ga_2O_3 was designed as a metal–semiconductor field-effect transistor (MESFET) showing excellent subthreshold swing of 68.9 and 84.6 mV/sec.[40] In addition, with the Ga_2O_3 exhibiting the second highest critical electric field and excellent critical breakdown strength of all wide bandgap semiconductors, a flexible high-power diode is realized using printed Ga_2O_3 on a plastic substrate. Under bending condition, a critical breakdown field strength of 1.07 MV cm^{-1} was recorded.[41] Meanwhile, the Ga_2O_3 could also be tapped as a promising candidate for ultra-high temperature gas sensing due to its high thermal and chemical stabilities that can allow a stable sensor operation at temperatures up to 1000 °C.[42-44] However, the detection of NO_x, based on Ga_2O_3 has rarely been studied, especially at temperatures above 500 °C. In terms of gas sensor performance, sensitivity is one of the most important figures of merit beside selectivity and stability of sensors. The sensitivity of a conductometric-type metal oxide semiconductor sensor is determined by measuring the change of resistance (conversely conductance) or current when target gas molecules interact with the sensor surface.[45] However, this type of gas sensors generally show lower sensitivity at high temperature due to usually unfavourable surface chemistries at high temperature.[46] Therefore, rational selections of sensor material and architecture design are critical for achieving highly sensitive and selective sensors at high temperature.

In this work, we have successfully developed a sensitive, robust, and low-cost nanorod-based gas sensor designed for monitoring NO_2 at high temperature, by utilizing perovskite oxide nanoparticle surface decoration on β-Ga_2O_3 nanorods. A drastic enhancement was observed in the enabled sensor performance by incorporation

of catalytical $La_{0.8}Sr_{0.2}CoO_3$ (LSCO) nanoparticles. A comparative study is conducted on the sensing properties of pristine β-Ga_2O_3 nanorod arrays and LSCO-nanoparticle-decorated β-Ga_2O_3 nanorod arrays, and we demonstrate the NO_2 sensitivity enhancement by an order of magnitude at 800 °C.

Results and Discussion

X-ray diffraction (XRD) patterns confirm that the initial hydrothermal growth yielded orthorhombic GaOOH (Figure 1a, top), and the following post annealing at 1000 °C finally converted GaOOH to monoclinic β-Ga_2O_3 (Figure 1a, bottom). The synthesized GaOOH nanorod array has a preferred growth direction perpendicular to (111); therefore, the intensity of (111) peak in XRD is stronger than that of (110) peak which is typically observed in GaOOH powders (JCPDS #06-0180).

Figure 1b is a typical energy dispersive x-ray spectroscopy (EDXS) spectrum of GaOOH nanorods with clearly revealed peaks of Ga and O from the nanorods and Si from the Si substrate. Figure 1c shows a typical cross-sectional SEM image of as-synthesized GaOOH nanorods grown perpendicular to the substrate with a length of ~1.8 μm. The top-view SEM images of the tips of GaOOH and Ga_2O_3 nanorods clearly display a uniform diamond shape with an average diagonal length of ~200 nm (Figures 1d and 1e).

Figure 1f shows a low-magnification TEM image of as-synthesized GaOOH with ~100 nm effective diameter. The corresponding selected area electron diffraction (SAED) pattern in the inset features a set of discrete diffraction spots, confirming the nanorod's single-crystalline nature with an orthorhombic structure (a = 4.58 Å, b = 9.8 Å, c = 2.97 Å). The GaOOH nanorod grows perpendicular to the (111) plane. The TEM image in Figure 1g displays an individual β-Ga_2O_3 nanorod with a diagonal width ~200 nm. The corresponding SAED pattern of the β-Ga_2O_3 nanorod confirms the monoclinic structure of β-Ga_2O_3 nanorod and its preferential growth orientation perpendicular to (001) plane.

The XRD patterns of Ga_2O_3 nanorod arrays decorated with two different nominal deposition thicknesses (3 nm vs. 8 nm) of LSCO nanoparticles are shown in Figure 2a, where most of the peaks match the monoclinic β-Ga_2O_3 and the SnO_2 seed layer. Meanwhile, the two strongest peaks from LSCO are too close to the peaks from SnO_2 to be differentiated from them. The corresponding top-view SEM images of LSCO-nanoparticle-decorated β-Ga_2O_3 nanorods reveal negligible difference compared with pure β-Ga_2O_3 nanorods with no apparently visible nanoparticle decoration (Figures 2b and 2c), indicating very small LSCO nanoparticle sizes to be resolved under the given SEM magnification. EDX spectrum shown in Figure 2d, however, clearly shows the presence of La, Sr, Co, O originating from the LSCO nanoparticle decoration, along with Ga and O from the nanorod cores.

A low-magnification bright-field STEM image in Figure 3a reveals a typical β-Ga_2O_3 nanorod of rough surface after LSCO nanoparticle
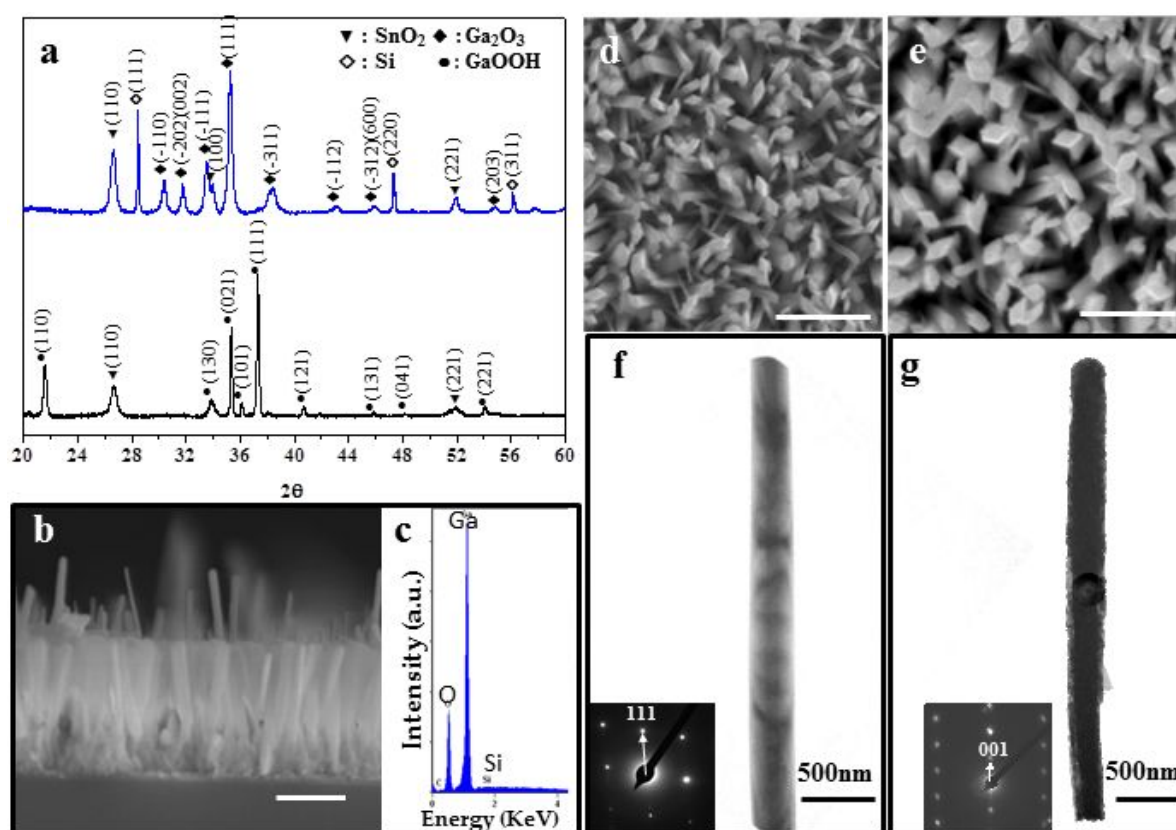
Figure 1. Structural characterization of β-Ga$_2$O$_3$ nanorod arrays: (a) X-ray diffraction (XRD) patterns of GaOOH (bottom) and β-Ga$_2$O$_3$ (top) nanorod arrays. (b) Cross-sectional view SEM image of GaOOH nanorod array, and (c) the corresponding energy dispersive X-ray (EDX) spectrum. Top view SEM images of (d) GaOOH and (e) Ga$_2$O$_3$ nanorods. (f) and (g): respective TEM images of a GaOOH nanorod, and a β-Ga$_2$O$_3$ nanorod, with insets being corresponding electron diffraction patterns. Scale bar: 1 µm.

decoration besides the nanorod mesoporous nature. The insets show the high-resolution lattice images of the LSCO decorated nanorod. LSCO nanoparticle with (110) plane is found at the nanorod surface layer, and β-Ga$_2$O$_3$ core is exposed with (002) planes. In Figures 3b–f, the elemental mapping displays strong and uniform intensities of Ga and O signals through the entire nanorod, while those of La, Sr, and Co are weakly revealed over the nanorod surface. The EDXS spectrum in Figure 3g confirms the presence of Ga and O from the nanorod, and La, Sr, and Co from the nanoparticle surface decoration.

The *in situ* NO$_2$ cyclic detection at 800 °C was employed to exploit the thermal stability of β-Ga$_2$O$_3$. It is worth pointing out that NO$_2$ is generally decomposed to NO and O$_2$ at high temperature region (>600 °C), and the conversion of NO$_2$ versus temperature is detailed in Figure S1, where the NO$_2$ starts to decompose to NO and O$_2$ at 432 °C, and the decomposition is completed at temperatures below 800 °C. As displayed in Figure 4a, the NO is stored typically in the form of bidentate nitrites and monodentate nitrite indicated by the strong bands at 1052 cm^{-1} and 1455 cm^{-1}, respectively. Besides, the strong bridging nitrates bands at 1229 cm^{-1} is probably ascribed to oxidation of nitrites by oxygen ions. However, with the presence of O$_2$, an oxidation reaction of nitrite to nitrate is clearly observed

(Figure 4b). The bidentate nitrites band is significantly weakened and monodentate nitrites still exist due to its stronger N=O bond. In addition, new peaks 1340 cm^{-1}, 1399 cm^{-1}, and 1630 cm^{-1} are ascribed to bidentate nitrate and monodentate nitrate, respectively. In comparison to NO$_2$ adsorption results (Figure 4c), only part of nitrite species (bidentate nitrite) is oxidized to nitrates in NO and O$_2$ co-adsorption scenario while monodentate nitrite may remain intact due to the stronger N=O bond. The impact of temperature on NO and O$_2$ co-adsorption is studied in the Figure S2. The intensity of all absorbed species on Ga$_2$O$_3$ changes obviously with the temperature. When temperature reaches 300 °C, a sharp decline in overall intensity is observed on the spectra. Generally, the activities of electrons are enhanced with increased temperature and more electrons are capable to promote the analytes adsorption after jumping over potential barrier. However, the enhancement of temperature may significantly boost thermal decomposition of the nitrates and nitrites, which results into the drastic decay of major peaks. The desorption of pre-adsorbed species was investigated by temperature-programmed desorption (TPD) spectra as shown in Figure S3. On the pristine Ga$_2$O$_3$ sample, a major peak is observed at around 383 °C, accounting for desorbed nitrates species. In addition, a weak NO$_2$ desorption peak centred approximate 121 °C is observed and ascribed to the removal of
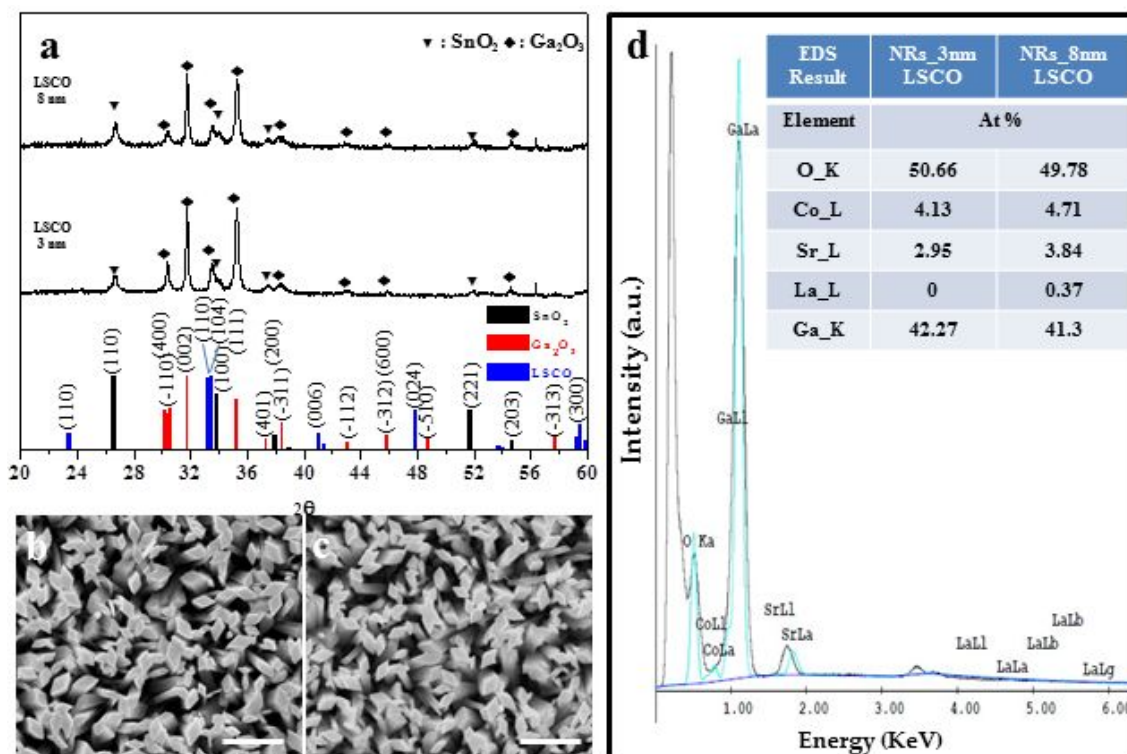
Figure 2. Morphology characterization of LSCO/β-Ga$_2$O$_3$ nanorod arrays: X-ray diffraction (XRD) patterns from (a) β-Ga$_2$O$_3$ nanorod arrays with 3 nm (middle) and 8 nm thick (top) LSCO nanoparticle deposition. A top-view SEM image of β-Ga$_2$O$_3$ nanorod arrays with (b) 3 nm, and (c) 8 nm LSCO nanoparticle decoration. (d) EDX spectrum of β-Ga$_2$O$_3$ nanorod arrays with 3 nm LSCO decoration, and the inset table is the composition analysis of β-Ga$_2$O$_3$ nanorod arrays with LSCO decorations.

weakly physiosorbed species.[47] Particularly, the desorption of nitrates or nitrites still occurred at 800 °C, indicating the remained nitrites and nitrates could still trigger the electrical response due to the narrowed conduction band. With the incorporation of LSCO, a new peak observed around 205 °C is assigned to desorption of nitrates in LSCO, indicating that NO$_2$ could also be stored in LSCO upon exposure to target analytes. The increased holes concentration may broaden electron depletion region in Ga$_2$O$_3$ and further enhance the response in comparison to pristine Ga$_2$O$_3$. The desorption peak centred around 452 °C in O$_2$ TPD spectra is ascribed to the desorption of oxygen ions (O$_2^-$ and O$^-$). It is worth pointing out that such peaks are also observed in NO$_2$ desorption spectra because O$_2$ is always added to help stabilize NO$_2$ in the NO$_2$ gas cylinders used for the testing.

A typical electrical response of the β-Ga$_2$O$_3$ nanorod array towards NO$_2$ in 800 °C is shown in Figure 5a as a function of time, where the NO$_2$ balanced in air are used as target analyte and pure air was used to drive the recovery of the sensor. Upon exposure to NO$_2$, the formation of gallium nitrites and nitrates may sharply decrease the free electron concentration, forming the charge depletion layer as indicated in Figure S4. The pure β-Ga$_2$O$_3$ nanorod array shows a fast, reproducible, and concentration-dependent increase in resistance (from ~5× to ~6×), confirming the functionality of β-Ga$_2$O$_3$ nanorod array for sensing NO$_2$ at high temperature. This is a remarkably high response compared with previously reported

resistive-type Ga$_2$O$_3$-based NO$_2$ gas sensors; for example, Jin et al. demonstrated multiple networked β-Ga$_2$O$_3$-based NO$_2$ gas sensor, but the response of pristine β-Ga$_2$O$_3$ toward NO$_2$ at 100 and 200 ppm was only about 1.47 and 1.76 (relative response is ~47 and 76%) at 300 °C, respectively.[48] Meanwhile, our data show that by purging with air, the resistance of β-Ga$_2$O$_3$ nanorod arrays could be fully reduced back to its base value, indicating a quick desorption of NO$_2$ molecules from the surface of β-Ga$_2$O$_3$ nanorod array. We also tested the cyclic response towards NO$_2$ balanced in nitrogen (Figure S5), and in this case, the response was slightly higher than that towards NO$_2$ balanced in air, which is likely due to the pre-adsorbed O$_2$ that can slightly increase the initial resistance. The observed response time (t$_{90}$) of the β-Ga$_2$O$_3$ nanorods, defined as the time when the normalized current change reaches 90% of the maximum response after NO$_2$ exposure, is 33 seconds towards 100 ppm NO$_2$, and it decreases for higher NO$_2$ concentrations (i.e., faster response). Overall, the Ga$_2$O$_3$ nanorod sensor response is fast at high temperature while displaying a negligible drift in the baseline for repeated operations. This improved baseline drift performance might be due to the high operation temperature that enables faster analyte adsorption and desorption kinetics.
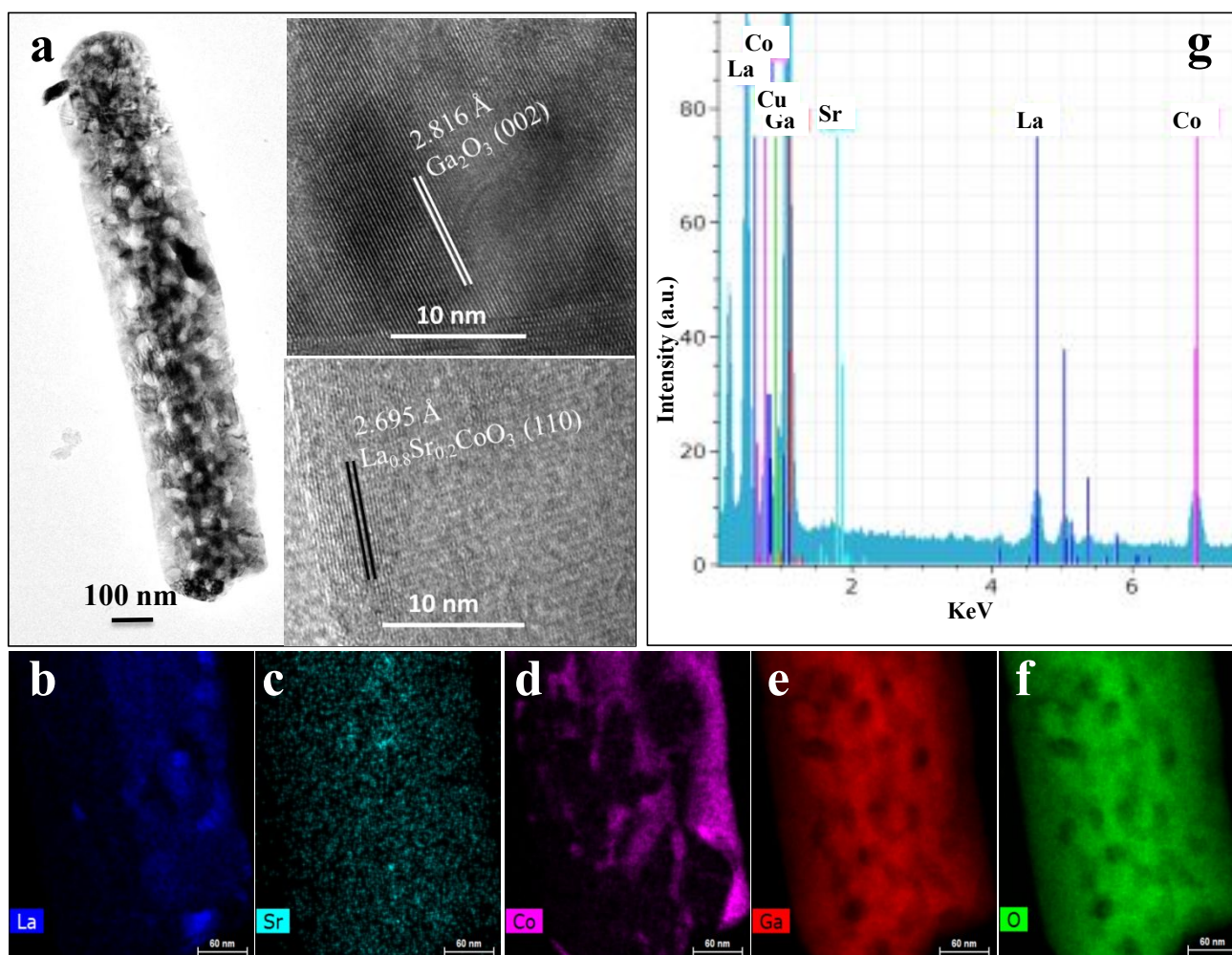
Figure 3. Structural characterization of LSCO/β-Ga$_2$O$_3$ nanorod arrays: (a) TEM image of a post annealing β-Ga$_2$O$_3$ nanorod coated with 8 nm LSCO decoration. The insets are the high-resolution images of coated LSCO nanoparticles on the surface (lower left corner) and β-Ga$_2$O$_3$ (upper right corner). (b)-(f) show the element mapping of 8 nm LSCO-coated β-Ga$_2$O$_3$ nanorod, presenting the element distribution of La, Sr, Co, Ga, O respectively. (g) The corresponding LSCO-coated β-Ga$_2$O$_3$ nanorod energy dispersive X-ray spectrum.

In detail, the consistently observed sensor response to NO$_2$ via the increase in resistance indicates that the majority charge carriers in our β-Ga$_2$O$_3$ are electrons (thus an n-type semiconductor sensor). The predominant point defects in β-Ga$_2$O$_3$ are oxygen vacancies, and they are known to be n-type dopant, generating free electrons via following mechanism:[49]

$$Ga_2O_3 \leftrightarrow 2Ga_{Ga}^x + 2O_O^x + V_O^* + e^- + \frac{1}{2}O_2 \qquad (1)$$
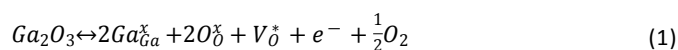
where Ga_{Ga}^x and O_O^x represent the regular lattice ions, while V_O^* is the charged defect with single ionized oxygen vacancy. It is worthy to note that the oxygen vacancies can also act as preferential adsorption sites for NO$_2$ molecules,[50, 51] facilitating the sensor response of the Ga$_2$O$_3$ nanorods. And the response in resistance of β-Ga$_2$O$_3$ nanorod array upon exposure to oxidizing gas NO$_2$ is generally explained by the formation of an electron depletion layer on the surface of nanorods.[16, 52] As NO$_2$ molecules may decompose

to NO and O$_2$, nitrites may be firstly formed, and then the bidentate nitrites would be oxidized to nitrate as described in the following reactions.

$$Ga_2O_3(V_O^*) + NO + e^- \rightarrow GaNO_2 \qquad (2)$$

$$Ga(NO_2)(bidentate) + O_2 \rightarrow GaNO_3 \qquad (3)$$
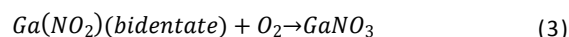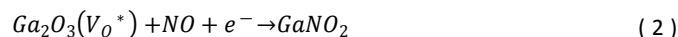
In addition, the decoration of catalytic LSCO nanoparticles on pristine β-Ga$_2$O$_3$ nanorods could greatly enhances the NO$_2$ gas sensing performance at high temperature (800 °C). The dynamic sensing characteristics of LSCO-nanoparticle-decorated β-Ga$_2$O$_3$ nanorod arrays under different NO$_2$ concentrations are shown in Figures 5b and 5c. We tested two different nominal thicknesses of LSCO nanoparticle deposition conditions (3 nm or 8 nm). Regardless of the thickness and tested NO$_2$ concentration, the NO$_2$ response of β-Ga$_2$O$_3$ nanorod arrays is enhanced over 500% with the LSCO nanoparticle decoration. The pristine β-Ga$_2$O$_3$ nanorod arrays shows
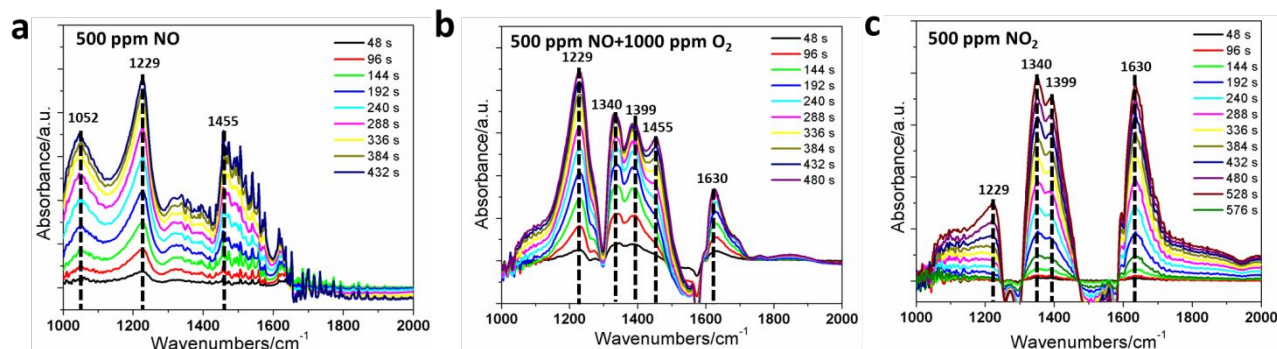
Figure 4. Time-resolved *in situ* DRIFTS study of adsorption of NO_2 on Ga_2O_3 at room temperature: (a) 500 ppm NO (b) 500 ppm NO + 1000 ppm O_2, and (c)500 ppm NO_2.

a base response ~5.12 at 200 ppm NO_2 exposure, while the response of 3 nm and 8 nm-LSCO-nanoparticle-decorated samples reach around 25.7 and 32.6, respectively (Figure 5d). Such high and reproducible response is excellent among the reported design for high temperature NO_2 detection shown in the Table 1. Meanwhile, thicker LSCO nanoparticle decoration (8 nm) appears to modestly increase the sensitivity (by ~ 10%) compared with 3 nm LSCO nanoparticle decoration, which is most likely resulted from too large nanoparticle surface coverage. The same trend was observed when NO_2 was balanced in N_2 as shown in Figures S4b-S4e. In the meantime, as indicated in Figures 5(e) and 5(f), the incorporation of LSCO facilitates the response with shorter response time but lengthens the recovery time. The slower sensor recovery might be due to a slower desorption kinetics of NO_2 (or NO_2^-) and corresponding nitrates and nitrites decomposition on the LSCO nanoparticle surface than that on β-Ga_2O_3. While the relatively faster desorption of NO_2 from the β-Ga_2O_3 nanorod surface primarily drives the decrease in resistance (i.e., main sensor recovery, via reduced depletion region) during the absence of NO_2, the relatively slower NO_2 desorption from the LSCO surface results in a residual temporal resistance and consequently lagged sensor recovery as the depletion region near the LSCO nanoparticles is relieved with a slower pace.

In addition to the significantly enhanced NO_2 sensitivity, the LSCO-nanoparticle decoration on Ga_2O_3 nanorod arrays also enables a faster temporal sensor response to a given NO_2 exposure compared with pristine Ga_2O_3 nanorod arrays. For instance, the sample with 8 nm LSCO nanoparticle decoration has a response time of ~5 seconds at the highest NO_2 concentration (300 ppm), which is about 60% shorter than that of pristine β-Ga_2O_3 nanorod arrays. The 3 nm LSCO-nanoparticle decoration also results in a similarly reduced response time (by ~67% and ~60% at NO_2 concentration of 100 and 300 ppm, respectively) (Figure 4d). Meanwhile, the recovery of β-Ga_2O_3 nanorod sensors at the absence of NO_2 becomes slower with the LSCO nanoparticle decoration by ~20%, compared with pristine β-Ga_2O_3 nanorod array sensors (Figure 4e). This might be due to the

different desorption kinetics of NO_2 on LSCO and Ga_2O_3 surfaces as discussed later.

Generally, the mesoporous distribution of LSCO decoration is revealed as discrete "islands" on the surface of Ga_2O_3 nanorods as indicated by TEM characterization, instead of a continuous layered structure. The LSCO nanoparticles are p-type semiconductor and the resulting p-n heterojunction with β-Ga_2O_3 should lead to the charge carrier diffusion between n-type β-Ga_2O_3 and LSCO, amplifying the overall n-type response of the heterostructure because the increased hole concentration in LSCO by analyte adsorption can drive a further electron diffusion (i.e., electron depletion) from β-Ga_2O_3 to LSCO. For the observed enhancement in the NO_2 sensitivity by LSCO nanoparticle decoration, the island-shape or mesoporous LSCO decoration should also provide higher surface area and more adsorption sites, which is significantly helpful in improving sensing performance.[53, 54] As indicated already, the p-n junction formed in LSCO/Ga_2O_3 interface region is another dominant mechanism responsible for the enhanced response.[55] Specifically, the formation of space charge region (i.e., depletion region) in β-Ga_2O_3 near the p-n junction interface with LSCO reduces the volume of conducting channel within the individual β-Ga_2O_3 nanorods. For a typical p-n junction, the width of space charge region is the sum of p-type region and n-type region.[56] Particularly, the n-type space charge region is connected to external circuit, and the conductivity of β-Ga_2O_3 is determined by the thickness of space charge region,[57]

$$x_d = x_n + x_p \tag{4}$$

ARTICLE

Table 1, Configuration and performance of various metal oxide semiconductor-based NO2 gas sensors for high-temperature NO_2 detection, where sensitivity is calculated based on Rg/Ra per ppm.

Materials	Nanostructure	Temperature range	Sensitivity(ppm^{-1})	Reference
$Cr-TiO_2$	Nanotube	300-500 °C	0.0023	[58]
LSFC/LSAIO	Film	700-800 °C	0.11	[59]
$YSZ/CoTa_2O_6$	Film	650 °C	0.32 mV/ppm	[60]
YSZ/In_2O_3	Film	700 °C	0.2~9 mV/ppm	[61]
Pyrochlore/$Sm_2Zr_2O_7$	Film	500-700 °C	0.06 µA/ppm	[62]
GaN	Nanowire	450-650 °C	0.002557	[63]
Gd0.2Sr0.8FeO3$-\delta$	Porous Film	500-800 °C	0.0038	[64]
YSZ/Pt	Film	700 °C	0.00036	[65]
$LSCO/Ga_2O_3$	Nanorod	800 °C	0.1625	This work

where x_d is the total thickness of depletion layer, x_n is thickness of depletion layer in n-type region, and x_p is thickness of depletion layer in p-type region.

The electric field varies linearly in the depletion region and reaches a maximum value at certain location and the maximum field can be expressed as

$$\varepsilon_{max} = -\frac{qN_ax_p}{\epsilon} = -\frac{qN_dx_n}{\epsilon} \qquad (5)$$

where N_d and N_a are the number of acceptors and donors

respectively, and ϵ represents the dielectric permittivity. And the relationship between x_p and x_n could be depicted as

$$N_dx_n = N_ax_p \qquad (6)$$

Combining the equations (5) and (6) yields

$$x_n = \frac{N_a}{N_d + N_a}x_d \qquad (7)$$

The total potential across the p-n junction must equal the difference between the built-in potential ϕ_i and the applied voltage V_a.

$$\phi_i - V_a = \frac{qN_ax_p^2}{2\epsilon} + \frac{qN_dx_n^2}{2\epsilon} \qquad (8)$$

Thus, the width of depletion layer in n-type region is obtained

$$x_n = \sqrt{\frac{2\epsilon N_a}{q}\frac{1}{N_dN_a + N_d}(\phi_i - V_a)} \qquad (9)$$

Upon exposure to oxidizing NO_2 molecules, the adsorption of NO_2 molecules occurs on the both surfaces of LSCO nanoparticles and uncovered β-Ga_2O_3. Especially, the unpaired electron of the NO_2 molecule reacts with the dangling bonds available on the LSCO nanoparticle surface, which in turn increases the free hole concentration in the valence band of LSCO.[66] The donors in Ga_2O_3 (i.e. oxygen vacancies) are consumed while the concentration of acceptors in LSCO increase, respectively. Thus, the enlarged difference in concentration of holes or electrons may drive the diffusion of electrons from Ga_2O_3 to LSCO and holes from LSCO to Ga_2O_3, which further decreases the concentration of electrons in

Ga_2O_3. Under constant external bias voltage, according to equation (8), increased N_a and decreased N_d may lead to thicker depletion layer in n-type region in comparison to pristine Ga_2O_3. This is the extra contribution to the intrinsic resistance increase of pristine Ga_2O_3 upon the NO_2 exposure, being responsible for the overall enhanced NO_2 sensitivity by the LSCO nanoparticle decoration. By the same explanation, it is natural that the increased surface coverage of LSCO nanoparticles (i.e., larger nominal thickness of LSCO deposition condition) further improves the NO_2 sensitivity of β-Ga_2O_3 nanorod arrays as we observed.

Finally, we demonstrate a highly selective sensing of NO_2 over O_2 using the LSCO-nanoparticle-decorated β-Ga_2O_3 nanorod array sensor. In addition to the sensitivity, the selectivity is another major challenge for gas sensors used in harsh industrial environments (e.g., high temperature, high pressure, highly corrosive, presence of contaminants or particulate matters, dynamic gas flow). Particularly, it becomes a key issue when there are multiple species of gas analytes with similar chemical natures. For example, O_2 is a well-known oxidizing gas that induces the increase in resistance (i.e., sensor response similar to NO_2) of n-type metal oxides upon the surface adsorption.[67, 68] In this study, we find that the LSCO-nanoparticle-decorated β-Ga_2O_3 nanorod array sensor clearly differentiates NO_2 from O_2 via highly distinguishable sensitivity and response time (Figure S6). The NO_2 sensitivity of LSCO-nanoparticle-decorated (8 nm) Ga_2O_3 nanorod array sensor is ~10 times larger than that toward O_2 at the same analyte concentration (300 ppm) (Figure S6b). Furthermore, there is a distinct difference in response time; the sensor response time for NO_2 only is 5 seconds while it is around 400 seconds for O_2. One possible reason for this difference in response time is the difference in adsorption energies between NO_2 and O_2 on the surfaces of LSCO and Ga_2O_3. The actual evaluation of the mentioned adsorption energies of NO_2 and O_2 is not covered by the current the scope of study, and further investigations are being planned to verify this hypothesis.
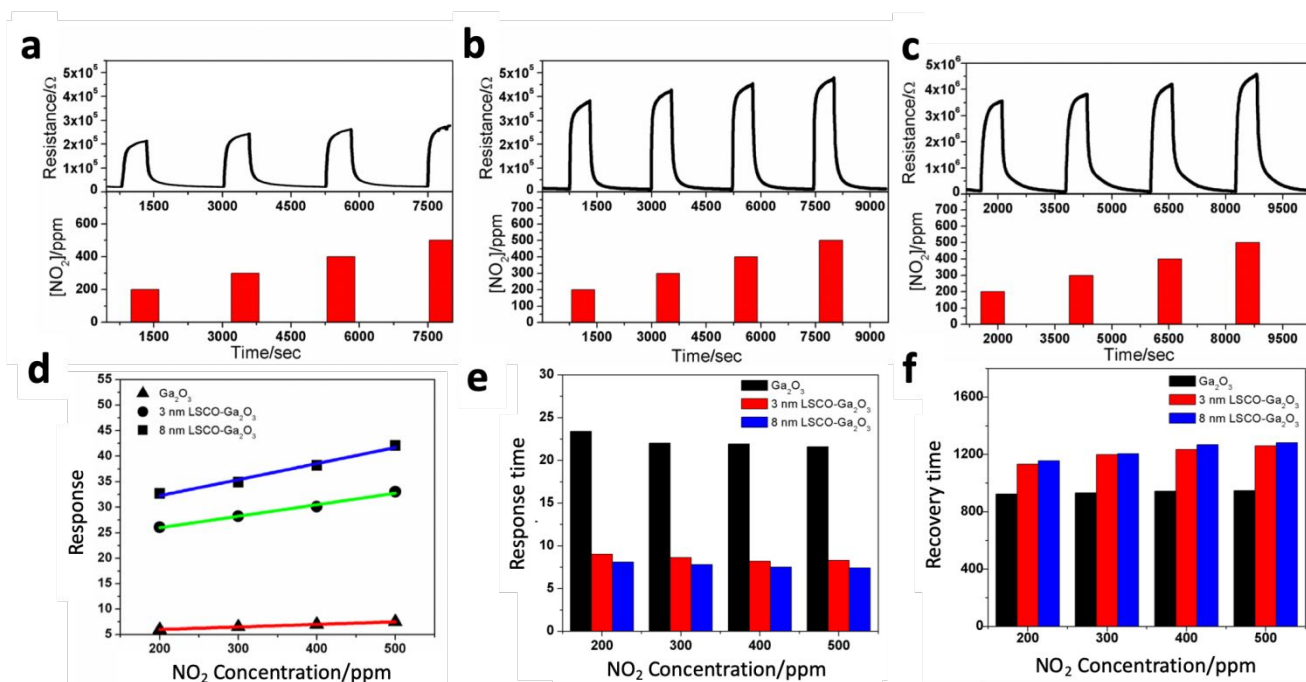
Experimental Methods:

Figure 5. NO_2 gas sensing performance of Ga_2O_3 nanorod: Dynamic response of (a) pure Ga_2O_3 nanorod array, (b) 3 nm LSCO/β-Ga_2O_3 , and (c) 8 nm LSCO/β-Ga_2O_3 tested at 800 °C with compressed air as background atmosphere and its corresponding NO_2 concentration; (d) Response, (e) Response time, and (f) Recovery time versus NO_2 concentrations characteristics of β-Ga_2O_3 and LSCO/β-Ga_2O_3 nanorod arrays tested at 800 °C.

Si wafers with (100) orientation and 1 μm SiO_2 insulator layer on top are used as substrates. Prior to Ga_2O_3 nanorod synthesis, the substrate was immersed in acetone solution and sonicated for 5 min, followed by sonication in deionized (DI) water for 5 min, which were repeated twice to remove the surface grease and organic deposits. High N_2 was used for blow-drying the Si wafer, which was then put on a hot plate at 80 °C for complete drying. Before growing nanorod arrays by hydrothermal synthesis, a 50 nm thick seed layer of SnO_2 was deposited on SiO_2/Si substrate by radio frequency (R.F.) magnetron sputtering, followed by post annealing at 900 °C for 2 h in ambient atmosphere to improve crystallinity. During the hydrothermal synthesis of nanorods, 0.6 g of Ga $(NO_3)_3·9H_2O$ was used as the precursor and fully dissolved in 40 mL DI water by stirring for 10 min. The prepared solution was poured into the Teflon bottle with SnO_2-seeded substrates, and sealed in the autoclave. The reaction temperature was kept at 150 °C for 12 h to grow GaOOH nanorod arrays. After hydrothermal growth, the samples were washed and rinsed by DI water and dried in air on a hot plate at 80 °C overnight. After air annealing at 1000 °C for 4 h, the as-grown GaOOH nanorods were finally converted into pure β-Ga_2O_3 nanorods.

Nanoparticles of La-based LSCO perovskite oxide were decorated on β-Ga_2O_3 nanorod arrays by R.F. magnetron sputtering method with controlled nominal thickness of 3 or 8 nm as monitored by a quartz microbalance. An X-ray diffractometer (Bruker D2 Phaser), a scanning electron microscope (SEM, JEOL JSM-6335F), a

transmission electron microscope (TEM, FEI T12), and a scanning transmission electron microscope (STEM, Talos F200X) were used to characterize the structure, morphology and composition of the nanorod array samples.

In situ diffuse reflectance infrared Fourier transform spectroscopy (DRIFTS) studies were carried out via Nicolet™ iS50 Fourier transform infrared spectroscopy (FTIR) spectrometer equipped with a tungsten-halogen white light source and its scanning wavenumbers window range from 400 to 4000 cm^{-1}. Each spectrum was recorded at a resolution of 2 cm^{-1} and 64 scans were averaged for sample spectrum resulting into a time resolution of 24 s. In each DRIFTS experimental section, 500 mg Ga_2O_3 powder sample (Fisher Sci.) was placed in the sample holder, and a filling bar was employed to achieve a reproducible reflecting plane. In the next step, the samples were tested through following procedure: 1) Purging with N_2 flow (30 mL/min) at 500 °C for 4 h, and then cooling down to room temperature in N_2 flow. 2） Background collection/recording in N_2 flow at room temperature. 3) Replacement of N_2 with target gas analytes (NO, NO_2 and $NO+O_2$) until achieving a saturated state. TPD experiments were carried out with Automated Catalyst Characterization System II 2920 (Micromeritics Inc.). In a typical run, 400 mg Ga_2O_3 or LSCO/Ga_2O_3 was put in a quartz U-shape microreactor. In the first step, the sample was pre-treated in Ar at 500 °C to remove the contamination and cooled to room temperature. Then, the sample was exposed in 200 ppm NO_2 and 1% O_2 for 2 h until a saturated

state was achieved. The spectrum was continuously recorded in TPD signal under Ar flow (25 cm^3/min) while the temperature was enhanced to 850 °C at 10 °C/min.

The resistor-type β-Ga$_2$O$_3$ nanorod array device was fabricated and tested in a high temperature tube furnace using a flow-through configuration. An alumina ceramic tube containing two through holes was used to hold and fix two Ni/Cr wires. As for the gas sensor device, the β-Ga$_2$O$_3$–based gas sensor was fixed on the alumina holder with two 10 μm thick platinum (Pt) wires, which were used as the electrodes of the gas sensor device. The Pt wires were connected the nanorod array gas sensor device with Ni/Cr wires, which were connected to a CHI 601C electrochemical workstation for recording the signal outputs continuously. The sensor circuit was subjected to a fixed 1 V direct current (DC) bias. The device was heated from room temperature to 800 °C in air with a ramp rate of 20 °C/min. The sensor device was placed and tested at the furnace centre. Gas sensing tests were performed under the exposure of NO$_2$ of varying concentration at 1 atm total pressure and 800 °C. The responses of the sensor to NO$_2$ were evaluated by measuring the current change upon exposure to NO$_2$ in a dynamic gas flow system under a gas flow rate of 1.5 L/min, which was regulated by a computer-controlled gas mixing system (S-4000, Environics Inc., USA). The air is used as the balance gas to monitor the response in practical air atmosphere. In addition, to better understand the sensing mechanism and investigate its selectivity over O$_2$, the cyclic tests in N$_2$ were conducted to eliminate the O$_2$ interference. The sensor response is defined by R_{NO2}/R_0, where R_{NO2} is the measured resistance of Ga$_2$O$_3$ nanorod device under NO$_2$ exposure, and R_0 is the initial resistance under balance air or N$_2$. All dynamic cyclic tests were carried out at 800 °C.

Conclusions

In summary, the perovskite LSCO-nanoparticle decoration enabled a highly enhanced NO$_2$ sensitivity in wide-bandgap β-Ga$_2$O$_3$ nanorod array gas sensors at high temperature with fast sensor response and high selectivity over O$_2$. The formation of p-n heterojunction is suggested to play major roles in the observed enhancement of sensor performances as it contributes to the modulation of depletion region with differentiated analyte desorption kinetics. These findings provide unique insight into rational design and development of high-performance gas sensors for oxidative gas pollutants at high temperatures.

Conflicts of interest

There are no conflicts to declare.

Acknowledgements

Notes and references

1. J. Khodakarami and P. Ghobadi, *Renewable Sustainable Energy Rev.*, 2016, **57**, 965-976.
2. W. Tsujita, A. Yoshino, H. Ishida and T. Moriizumi, *Sens. Actuators, B*, 2005, **110**, 304-311.
3. H. J. Kim, J. W. Yoon, K. I. Choi, H. W. Jang, A. Umar and J. H. Lee, *Nanoscale*, 2013, **5**, 7066-7073.
4. A. Kumar, H. Kim and G. P. Hancke, *IEEE Sens. J.*, 2013, **13**, 1329-1339.
5. C. J. Stevens, *Science*, 2019, **363**, 578-580.
6. J. Kašpar, P. Fornasiero and N. Hickey, *Catalysis today*, 2003, **77**, 419-449.
7. H. L. Tuller, *Sens. Actuators, B*, 2013, **187**, 106.
8. J. W. Fergus, *Sens. Actuators, B*, 2007, **122**, 683.
9. J. W. Fergus, *Sens. Actuators, B*, 2007, **123**, 1169.
10. J. W. Fergus, *Sens. Actuators, B*, 2007, **121**, 652.
11. A. Afzal, N. Cioffi, L. Sabbatini and L. Torsi, *Sens. Actuators, B*, 2012, **171-172**, 25-42.
12. A. M. Ruiz, G. Sakai, A. Cornet, K. Shimanoe, J. R. Morante and N. Yamazoe, *Sens. Actuators, B*, 2003, **93**, 509-518.
13. G. Lu, N. Miura and N. Yamazoe, *J. Mater. Chem.*, 1997, **7**, 1445-1449.
14. L. You, X. He, D. Wang, P. Sun, Y. F. Sun, X. S. Liang, Y. Du and G. Y. Lu, *Sens. Actuators, B*, 2012, **173**, 426-432.
15. A. Sharma, M. Tomar and V. Gupta, *Sens. Actuators, B*, 2011, **156**, 743-752.
16. H. T. Giang, H. T. Duy, P. Q. Ngan, G. H. Thai, D. T. A. Thu, D. T. Thu and N. N. Toan, *Sens. Actuators, B*, 2013, **183**, 550-555.
17. Y. Li, W. Wlodarski, K. Galatsis, S. H. Moslih, J. Cole, S. Russo and N. Rockelmann, *Sens. Actuators, B*, 2002, **83**, 160-163.
18. H. Huang, S. Tian, J. Xu, Z. Xie, D. Zeng, D. Chen and G. Shen, *Nanotechnology*, 2012, **23**, 105502.
19. Q. Wan and T. H. Wang, *Chem. Commun.*, 2005, DOI: 10.1039/b504094a, 3841-3843.
20. P. Rai, Y.-S. Kim, H.-M. Song, M.-K. Song and Y.-T. Yu, *Sens. Actuators, B*, 2012, **165**, 133-142.
21. R. K. Joshi, Q. Hu, F. Alvi, N. Joshi and A. Kumar, *J. Phys. Chem. C*, 2009, **113**, 16119-16202.
22. A. Kolmakov, D. O. Klenov, Y. Lilach, S. Stemmer and M. Moskovits, *Nano Lett.*, 2005, **5**, 667-673.
23. R. Xing, Q. Li, L. Xia, J. Song, L. Xu, J. Zhang, Y. Xie and H. Song, *Nanoscale*, 2015, **7**, 13051-13060.
24. P. Rai, R. Khan, S. Raj, S. M. Majhi, K. K. Park, Y. T. Yu, I. H. Lee and P. K. Sekhar, *Nanoscale*, 2014, **6**, 581-588.
25. D. R. Miller, S. A. Akbar and P. A. Morris, *Sens. Actuators, B*, 2014, **204**, 250-272.
26. J. X. Wang, X. W. Sun, Y. Yang, K. K. Kyaw, X. Y. Huang, J. Z. Yin, J. Wei and H. V. Demir, *Nanotechnology*, 2011, **22**, 325704.
27. N. Wu, M. Zhao, J.-G. Zheng, C. Jiang, B. Myers, S. Li, M. Chyu and S. X. Mao, *Nanotechnology*, 2005, **16**, 2878-2881.

28. L. Li, C. Zhang and W. Chen, *Nanoscale*, 2015, **7**, 12133-12142.

29. Z. L. Wang, J. M. Petroski, T. C. Green and M. A. El-Sayed, *J. Phys. Chem. B*, 1998, **102**, 6145-6151.

30. H.-J. Lin, J. P. Baltrus, H. Gao, Y. Ding, C.-Y. Nam, P. Ohodnicki and P.-X. Gao, *ACS Appl. Mater. Interfaces*, 2016, **8**, 8880-8887.

31. C. A. Hancock, J. M. Porras-Vazquez, P. J. Keenan and P. R. Slater, *Dalton Trans.*, 2015, **44**, 10559-10569.

32. M. H. Rubel, A. Miura, T. Takei, N. Kumada, M. Mozahar Ali, M. Nagao, S. Watauchi, I. Tanaka, K. Oka, M. Azuma, E. Magome, C. Moriyoshi, Y. Kuroiwa and A. K. Azharul Islam, *Angew. Chem., Int. Ed. Engl.*, 2014, **53**, 3599-3603.

33. B. Yan, M. Jansen and C. Felser, *Nat. Phys.*, 2013, **9**, 709-711.

34. M. Staruch, H. Gao, P.-X. Gao and M. Jain, *Adv. Funct. Mater.*, 2012, **22**, 3591-3595.

35. H. Gao, M. Staruch, M. Jain, P.-X. Gao, P. Shimpi, Y. Guo, W. Cai and H.-J. Lin, *Appl. Phys. Lett.*, 2011, **98**, 123105.

36. Z. Galazka, *Semiconductor Science and Technology*, 2018, **33**, 113001.

37. L.-X. Qian, Z.-H. Wu, Y.-Y. Zhang, P. T. Lai, X.-Z. Liu and Y.-R. Li, *ACS Photonics*, 2017, **4**, 2203-2211.

38. N. Blumenschein, T. Paskova and J. F. Muth, *PHYSICA STATUS SOLIDI A-APPLICATIONS AND MATERIALS SCIENCE*, 2019, **216**.

39. B. R. Tak, V. Gupta, A. K. Kapoor, Y.-H. Chu and R. Singh, *ACS Applied Electronic Materials*, 2019, **1**, 2463-2470.

40. J. Kim and J. Kim, *ACS Applied Materials & Interfaces*, 2020.

41. E. Swinnich, M. N. Hasan, K. Zeng, Y. Dove, U. Singisetti, B. Mazumder and J. H. Seo, *Advanced Electronic Materials*, 2019, **5**, 1800714.

42. M. Bartic, M. Ogita, M. Isai, C.-L. Baban and H. Suzuki, *J. Appl. Phys.*, 2007, **102**, 023709.

43. U. Hoefer, J. Frank and M. Fleisher, *Sens. Actuators, B*, 2001, **78**, 6-11.

44. T. Schwebel, M. Fleischer, H. Meixner and C.-D. Kohl, *Sens. Actuators, B*, 1998, **49**, 46-51.

45. C. Wang, L. Yin, L. Zhang, D. Xiang and R. Gao, *Sensors*, 2010, **10**, 2088-2106.

46. Y. Liu, J. Parisi, X. Sun and Y. Lei, *J. Mater. Chem. A*, 2014, **2**, 9919-9943.

47. F. Prinetto, G. Ghiotti, I. Nova, L. Lietti, E. Tronconi and P. Forzatti, *The Journal of Physical Chemistry B*, 2001, **105**, 12732-12745.

48. C. Jin, S. Park, H. Kim and C. Lee, *Sens. Actuators, B*, 2012, **161**, 223-228.

49. M. Bartic, C.-I. Baban, H. Suzuki, M. Ogita and M. Isai, *J. Am. Ceram. Soc.*, 2007, **90**, 2879-2884.

50. S. Maeng, S. W. Kim, D. H. Lee, S. E. Moon, K. C. Kim and A. Maiti, *ACS Appl. Mater. Interfaces*, 2014, **6**, 357-363.

51. M. Epifani, J. D. Prades, E. Comini, E. Pellicer, M. Avella, P. Siciliano, G. Faglia, A. Cirera, R. Scotti, F. Morazzoni and J. R. Morante, *J. Phys. Chem. C*, 2008, **112**, 19540-19546.

52. Y. Gönüllü, A. A. Haidry and B. Saruhan, *Sens. Actuators, B*, 2015, **217**, 78-87.

53. M. Mashock, K. Yu, S. Cui, S. Mao, G. Lu and J. Chen, *ACS applied materials & interfaces*, 2012, **4**, 4192-4199.

54. L. T. Hoa and S. H. Hur, *physica status solidi (a)*, 2013, **210**, 1213-1216.

55. A. Sharma, M. Tomar and V. Gupta, *Sens. Actuators, B*, 2013, **181**, 735-742.

56. R. F. Pierret, *Semiconductor device fundamentals*, Pearson Education India, 1996.

57. S. M. Sze and K. K. Ng, *Physics of semiconductor devices*, John wiley & sons, 2006.

58. Y. Gönüllü, A. A. Haidry and B. Saruhan, *Sensors and Actuators B: Chemical*, 2015, **217**, 78-87.

59. L. Dai, M. Shi, W. Han, W. Meng, Z. He, L. Zhu and L. Wang, *Sensors and Actuators B: Chemical*, 2017, **250**, 629-640.

60. F. Liu, B. Wang, X. Yang, Y. Guan, Q. Wang, X. Liang, P. Sun, Y. Wang and G. Lu, *Sensors and Actuators B: Chemical*, 2017, **240**, 148-157.

61. F. Liu, Y. Guan, H. Sun, X. Xu, R. Sun, X. Liang, P. Sun, Y. Gao and G. Lu, *Sensors and Actuators B: Chemical*, 2016, **222**, 698-706.

62. Y. Zheng, P. Duan, Z. Li, G. Cai, F. Zhong and Y. Xiao, *Journal of the European Ceramic Society*, 2020.

63. J. Sim, K. Kim, S. Song and J. Kim, *Analyst*, 2013, **138**, 2432-2437.

64. L. Wang, Y. Wang, L. Dai, Y. Li, J. Zhu and H. Zhou, *Journal of alloys and compounds*, 2014, **583**, 361-365.

65. N. Miura, M. Nakatou and S. Zhuiykov, *Sensors and Actuators B: Chemical*, 2003, **93**, 221-228.

66. S. Thirumalairajan, K. Girija, V. R. Mastelaro and N. Ponpandian, *ACS Appl. Mater. Interfaces*, 2014, **6**, 13917-13927.

67. Y. Xu, X. Zhou and O. T. Sorensen, *Sens. Actuators, B* 2000, **65**, 2-4.

68. Z. Liu, T. Yamazaki, Y. Shen, T. Kikuta, N. Nakatani and Y. Li, *Sens. Actuators, B*, 2008, **129**, 666-670.